Journal of Non-Crystalline Solids 582 (2022) 121458

Contents lists available at ScienceDirect

Journal of Non-Crystalline Solids

journal homepage: www.elsevier.com/locate/jnoncrysol

Fabrication of amorphous and high-entropy biphasic composites using high-frequency ultrasonic vibration

Xiong Liang, Kai Wu, Jianan Fu, Luyao Li, Caitao Fan, Wenxin Wen, Wenqing Ruan, Shuai Ren, Zhenxuan Zhang, Jiang Ma *

Shenzhen Key Laboratory of High Performance Nontraditional Manufacturing, College of Mechatronics and Control Engineering, Shenzhen University, Shenzhen, 518060, China

ARTICLE INFO

Keywords:
Amorphous alloy
High entropy alloy
Composites
Ultrasonic vibration

ABSTRACT

With the adoption of a high-frequency ultrasonic vibration method, we successfully fabricated the composites of amorphous and high-entropy alloys. The low-temperature and low-stress method enables us to fabricate composites which unite both crystalline and amorphous properties. Through adjusting the mass ratios of amorphous and high-entropy alloys in the composites, the regulation of the properties of the composites was achieved. Microscopic observations demonstrate that the composites of all proportions exhibit good bonding quality without the existence of pores or cracks. Due to the mixture of amorphous and crystalline phase, the mechanical properties of the composites were optimized compared to that of the pure single-phase materials. Our results provide ideas for the design and fabrication of composite materials containing multiphase and multi-component with specific properties.

1. Introduction

As a consequence of their unique amorphous structure, amorphous alloys, also known as metallic glasses (MGs), possess many potential applications in industry[1–8]. Because of their considerable strength[9], corrosion resistance[10, 11], toughness[12], hardness[13], wear resistance[14], catalysis[15] and super plasticity[16] compared to traditional crystalline materials, since the first discovery of MGs in 1960[17], MGs have received great attention from material researchers, and thus trigger a large number of studies and reports. Meanwhile, another series of multi-principal element materials, namely high entropy alloys (HEAs), have also attracted extensive interests owing to their unique microstructure and properties[18].

Compared with traditional crystalline alloy, some high-entropy alloys have exceptional corrosion resistance, oxidation resistance, great ductility, and high tensile strength[19–29], and can especially exhibit excellent mechanical properties under some extreme conditions[30]. Since the 1910s[31], high-entropy alloys have been regarded as a research hotspot as a result of their potential for applications in material science and engineering. Theoretically, the fabrication of composites of amorphous alloys and high-entropy alloys is possible to integrate the superiority of both and simultaneously compensate for the defects of a single material. There have been reports of ex-situ metallic glass matrix composites (MGMCs) with improved toughness obtained by adding a second solid-state phase to the liquid state of the MG alloy. The second phase added to the glass matrix can be ductile metallic [32] or brittle intermetallic/ceramic particles/fibers. As MGMCs have better mechanical performance compared to the monolithic MGs, developing new techniques to fabricate MGMCs can be of paramount importance from both the scientific and technological points of view [33].

Recently, an ultrasound-assisted forming method for amorphous alloys[34–37] has been proposed, which turn out to be novel and ideal for the fabrication of the composites of MG and HEA in this study. Normally, most amorphous alloys present nearly no plasticity at room temperature, which greatly hinders their plastic forming using traditional processing methods. Therefore, the achievement of super-plasticity of amorphous alloy is the basis of the fabrication of the composites of MG and HEA. Traditional method to process MGs is normally conducted within their supercooled liquid region (SLR), which is known as “thermal-plastic” forming (TPF) at high temperature. To develop extensive homogeneous plastic flows while avoid crystallization, the selection of MGs composition and the protocol for thermal treatment subjects to limitations. During the TPF process, the intrinsic structures and mechanical properties would be degenerated obviously. By contrast, homogeneous

---

* Corresponding author.
E-mail address: majiang@szu.edu.cn (J. Ma).

https://doi.org/10.1016/j.jnoncrysol.2022.121458
Received 25 October 2021; Received in revised form 15 January 2022; Accepted 26 January 2022
0022-3093/

super-plasticity can occur rapidly in different MGs at room temperature when subjected to ultrasonic agitations in seconds. The super-plasticity is attributed to dynamic heterogeneity and cyclic induced atomic-scale dilations in MGs, which leads to significant rejuvenation and final collapse of the solid-like amorphous structure, thereby leading to an overall fluid-like behaviour. The ability of amorphous alloys to soften and flow to a specific shape under high-frequency ultrasonic vibration enables MGs to yield super-plasticity flow and "ultrasound plastic" forming near room temperature through ultrasonic liquefaction. In this study, we have successfully fabricated composites of amorphous alloy and high-entropy alloy which unite both crystalline and amorphous properties at low temperature and low pressure. Additionally, through the adjustment of the proportion that amorphous and high-entropy alloys account for in the composites, we have been able to regulate the properties of the composites to achieve better mechanical performance than pure single-phase materials.

2. Material and methods

2.1. Materials

Amorphous alloy $La_{55}Al_{25}Ni_{5}Cu_{10}Co_{5}$ (at%) and high entropy alloy $Co_{20}Cr_{20}Fe_{20}Ni_{20}Mn_{20}$ (at%) powders were used as raw materials in this experiment. The reasons for adopting La-based MG include its wide supercooled liquid region (SLR), which is important to retain its amorphous structure under high frequency ultrasonic vibration, more importantly, its ultrasonic plasticity and glass forming ability are crucial to guarantee its binding with HEA. Similarly, the potential property under applied ultrasonic vibration and the prominent plasticity of $Co_{20}Cr_{20}Fe_{20}Ni_{20}Mn_{20}$ make it a good option for the study. The high entropy alloy powder was prepared by vacuum arc melting and real air atomization process, and the amorphous alloy was prepared by vacuum arc melting and high vacuum single-roller belt dumping and mechanical crushing process. In the experiments, the amorphous alloy and the high entropy alloy powder were mixed in the mass ratios of 8:2, 7:3, 6:4, 5:5, and 4:6 respectively.

2.2. Characterization

The intrinsic properties of amorphous alloy, high entropy alloy and their composites were determined by X-ray diffractometer (XRD; Rigaku miniflex 600, Japan) with Cu Kα radiation. The micromorphology of the composites before and after compression experiments was observed by scanning electron microscope (SEM; FEI QUANTA FEG 450, USA). The dimension and characteristics of defects that may exist inside the composites were characterized using a three-dimensional computed tomography system (CT, Sanying precision instruments-nano Voxel 3000d, China). A microhardness tester (FM- ARS9000 Japan) was used to analyse and compare the microhardness of amorphous alloys, high entropy alloys and composites. The electron diffraction patterns and energy dispersive spectrometry were conducted using a transmission electron microscopy (TEM; FEI-Titan3-themisg2, USA). The nanoscale mechanical properties were tested by a nanoindentation testing system (Hysitron TI 950, Bruker, Germany) with a Berkovich tip.

2.3. Experimental setup

A schematic diagram of the fabrication of amorphous alloy and high entropy alloy composites is shown in Fig. 1(a). Specifically, the mixed powder was firstly compacted under the pre-pressure provided by a horn without the application of ultrasound, and later the compacted powder was continuously pressed for several seconds under the horn with high-frequency ultrasound (~20,000 Hz). During this process, the amorphous alloy underwent softening and plastic flow and bonded into a bulk mass with the high entropy alloy wrapped inside, resulting in the formation of a complete block. Based on the ultrasonic vibration method, we achieved the regulation of the structure and property of the composites through adjusting the mass ratio of amorphous alloy and high-entropy alloy. By altering the composition and content of raw materials, we are even able to artificially design and prepare materials containing

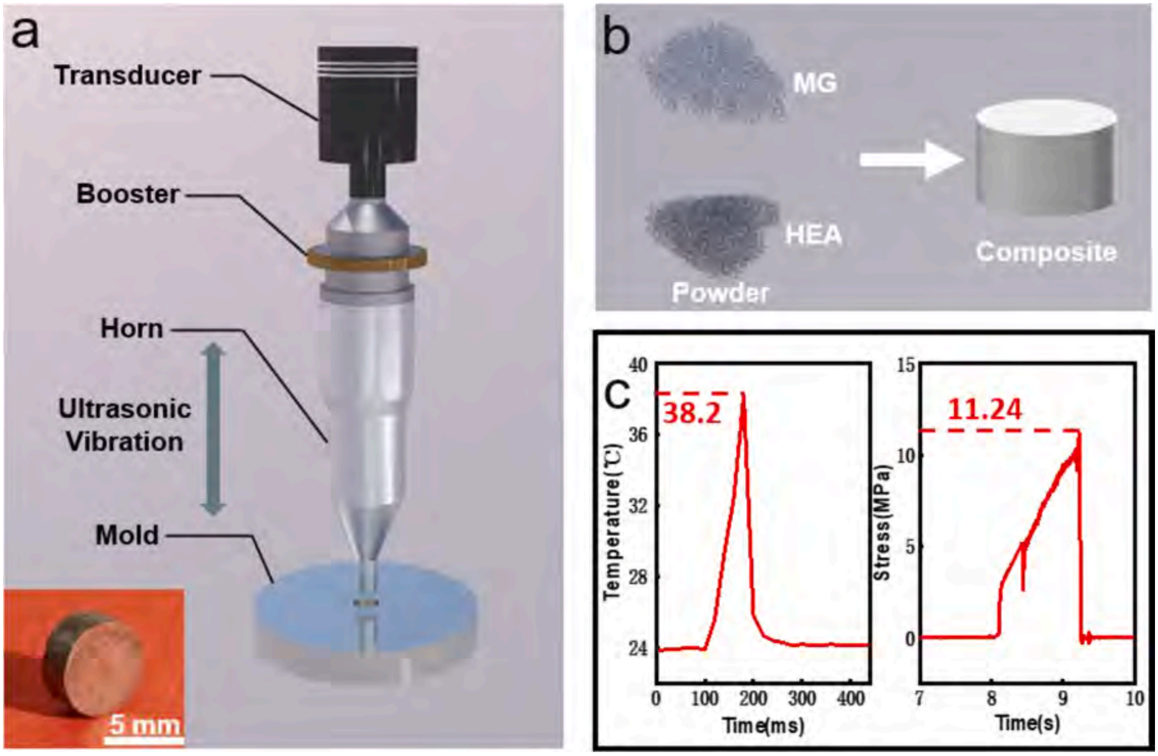

Fig. 1. (a) A schematic diagram for fabricating the HEA and MG composites, the inset is the HEA and amorphous alloy composite. (b) A schematic diagram of the HEA and MG powder and their composite. (c) The parameters applied during the ultrasonic vibration.

multi-phase and multi-component functional gradients with specific properties according to the requirements. During the ultrasonic vibration experiments, the temperature rise and pressure values imposed on the samples were also determined.

3. Results and discussion

3.1. Amorphous and high-entropy alloy composites

In the above-mentioned experiments, we successfully obtained composites of amorphous and high-entropy alloys. Fig. 1(a) shows composite block with a diameter of ~5 mm and a thickness of ~3 mm, with a distinct metallic luster on the block surface. The size of the sample varies with the altering of the mold size and experimental parameters. The temperature and pressure profiles during ultrasonic vibration of the 5:5 composite are given in Fig 1 (c) as representative. As can be seen, the maximum temperature rise in the composite is as small as 38.2 ^{o}C which is far lower than the glass transition temperature of the La-based MG matrix which is (190 ^{o}C). Further, it is evident from Fig. 1 (c) that the applied pressure during the ultrasonic process is ~11 MPa, being quite smaller than the yield stress of the HEA which is determined to be 160 MPa. These findings highlight the advantages of the ultrasonic vibration technique to fabricate MGMCs compared to the conventional approaches where high temperatures/pressures are required to fabricate MGMCs.

3.2. Intrinsic properties and microscopic morphology

The intrinsic characteristics of amorphous alloys, high entropy alloys and composites were determined using XRD. Fig. 2(a) shows the XRD patterns of amorphous alloys, high entropy alloys, and the composites. It is clear that the XRD pattern of all composites consist of amorphous and crystalline peaks, and the intensity of the amorphous peaks ascends as the proportion of amorphous alloys in the composites increases, indicating amorphous structure of MG in the composites remains unchanged. Fig. 2(b)-(k) show the cross-sectional morphology of the composites after compression test. The content of spherical particles which proves to be HEA in the SEM morphology of the cross-section increases as the mass ratio of high-entropy alloys in the composites improves. Furthermore, it can be seen from the SEM images that HEA particles are embedded into the composites, showing stable bonding of MG and HEA after ultrasonic vibration.

3.3. EDS and electron diffraction pattern

The elemental distribution of the composites was determined by energy dispersive spectrometer to figure out how amorphous and high entropy alloys were distributed and bonded in the composites. Fig. 3(o) illustrates the elemental distribution of the composite in the microscopic region where the amorphous and high entropy alloys are bound. In the region enriched in La, Al, and Cu elements, the chemical composition should be $LA_{55}Al_{25}NI_{5}Cu_{10}Co_{5}$, and in the region enriched in Cr, Fe, and

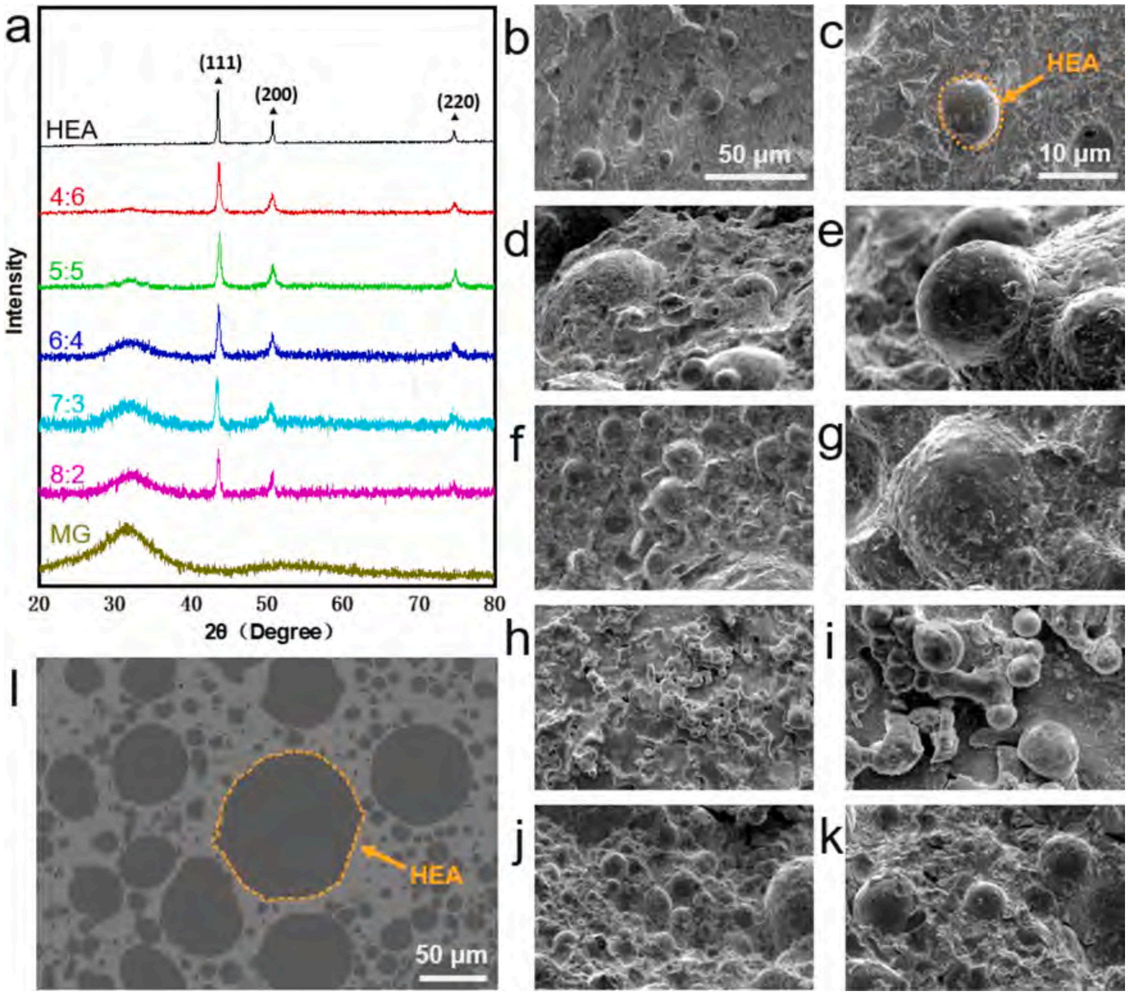

Fig. 2. (a) The XRD patterns of HEA, amorphous alloy and their composites. (b)-(k) show the cross-sectional SEM images of the composites after compression, the mass ratio of MG and HEA of the composites is 8:2, 7:3, 6:4, 5:5, 4:6 respectively from top to bottom. (l) The overall SEM image of the observed 5:5 composite.

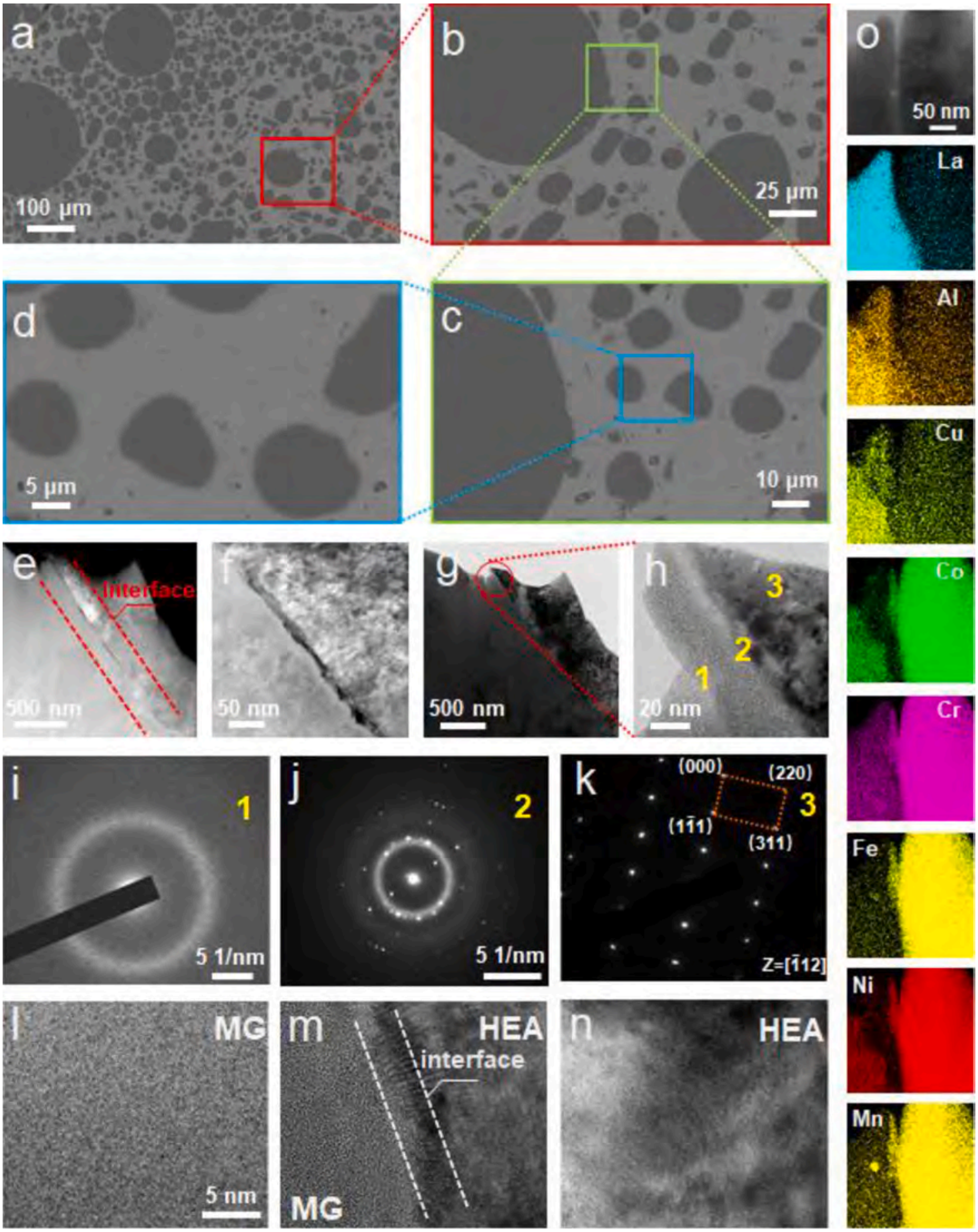

Fig. 3. (a)-(d) The SEM images of the fabricated 5:5 composite under magnification levels of 500×, 2000×, 4000×, 8000×. (e) The dark-field TEM image of the bonding area. (f) The local enlarged image of (e). (g) The bright-field TEM image of the bonding area. (h) The local enlarged image of (g). (i)-(k) The diffraction patterns which correspond to regions 1, 2, and 3 in (h). (l)-(n) The high-resolution TEM images from regions 1, 2, and 3 in (h), respectively representing the pure MG phase, MG and HEA binding phase, and the pure HEA phase. (o) The elemental distributions in a micro-region that contains both MG and HEA phase.

Mn elements, the chemical composition should be $Co_{20}Cr_{20}Fe_{20}Ni_{20}Mn_{20}$. Further, the elemental maps obviously show that the chemical elements interdiffuse and this atomic transfer between different elements yield the bonding between the MG matrix and the HEA particle.

To further investigate the internal structure of the composites, we determined the binding interface of the amorphous alloy and the high entropy alloy, and cut there with FIB. The interface was then observed by transmission electron microscopy. Fig. 3(e-h) show the dark-field and bright-field images of the interface and the surrounding regions. Three different contrasts can be detected from the TEM images, being marked as regions 1, 2, and 3 in Fig. 3(h). The selected area electron diffraction (SAED) patterns of these regions are shown in Fig. 3(i-k). It is evident from Fig. 3(i) that the region 1 has a typical diffraction halo ring, indicating that this region is a pure amorphous region and that the amorphous alloy retains its amorphous structure after high-frequency ultrasonic vibration. For the interface region (region 2), the diffraction pattern (Fig. 3(j)) exhibits both a halo and crystalline diffraction spots, indicating that this region is where amorphous alloy is combined with high entropy alloy. In the region 3 (Fig. 3(k)), the diffraction halo disappears and there remain only diffraction spots, indicating that this region is a pure high entropy region. These gradual changes in diffraction patterns reflect the binary phase composition of the composites. The binary phase composition can also be determined from the comparison of the dark field image and bright field images. The high-resolution TEM images (Fig. 3(l-n)) also confirm that while regions 1 and 3 respectively are purely amorphous and purely crystalline, the interface region contains both the amorphous and crystalline phases.

3.4. Defects and bonding quality analysis

In order to detect whether defects exist inside the composite, the samples were observed at different magnification levels using SEM. As can be seen from Fig. 3(a-d), the samples display good compactness, no pores and cracks are observed on the surface at the magnification levels of 500×, 2000×, 4000×, and 8000×, demonstrating the fine bonding quality of the composites. Besides, a high-resolution computed tomography system with an actual spatial resolution of 0.5 μm was applied for the three-dimensional visual characterization of the sample interior. Owing to the high voltage X-ray source with a micro-focal and highly sensitive detector, the CT clearly displays the sample interior. Fig. 4 shows the CT scanning images of the composites from the outer edge to the center at different cutting positions. The tomography images demonstrate the bonding state of the amorphous alloy and the high-entropy alloy. No obvious defects are seen inside the samples. In addition. Density is also a convincing index to further evaluate the bonding quality of the composites. During the experiment, Archimedes' principle was adopted to make a comparison of the actual and theoretical density of MG, HEA and the composites. The actual density of the MG, HEA and composites should be calculated by the equation: $\rho_{\text{actual}} = (\omega_1 \times \rho_1)/(\omega_1 - \omega_2)$, in which ρ_{actual} represents the actual density of the object, while ρ_1 represents the density of distilled water whose value is supposed to be 0.999 g/cm^3 at room temperature, and ω_1, ω_2 represent the weight of the object in air and distilled water respectively. The theoretical density of the composites should be calculated by the following equation:

$$\rho_{\text{composites}} = \frac{(\omega_{\text{MG}} + \omega_{\text{admixture}})}{(\omega_{\text{MG}}/\rho_{\text{MG}} + \omega_{\text{admixture}}/\rho_{\text{admixture}})} \tag{1}$$

In equation (1), the mean value of the actual density of as-cast MG and HEA obtained from repeated measurement is 5.72505 g/cm^3 and 7.87857 g/cm^3, and that of the composites of which the mass ratio of MG and HEA is 8:2, 7:3, 6:4, 5:5, 4:6 is 5.84653, 6.03541, 6.28892, 6.50065, 6.71098 g/cm^3 respectively. Specially, the mean value of the actual density of MG obtained from vibrated powder is 5.42863. The corresponding value of the theoretical density of the composites is 5.79077, 5.90168, 6.06484, 6.21972, 6.39575 g/cm^3. By comparing the values of the actual densities and theoretical densities, one can realize that as the volume fraction of the HEA particles in the composite increase, the difference between the theoretical and actual densities gets larger. This trend suggests that some residual porosity may exist in the composite which is proportional to the increase in interfacial area between the HEA and MG.

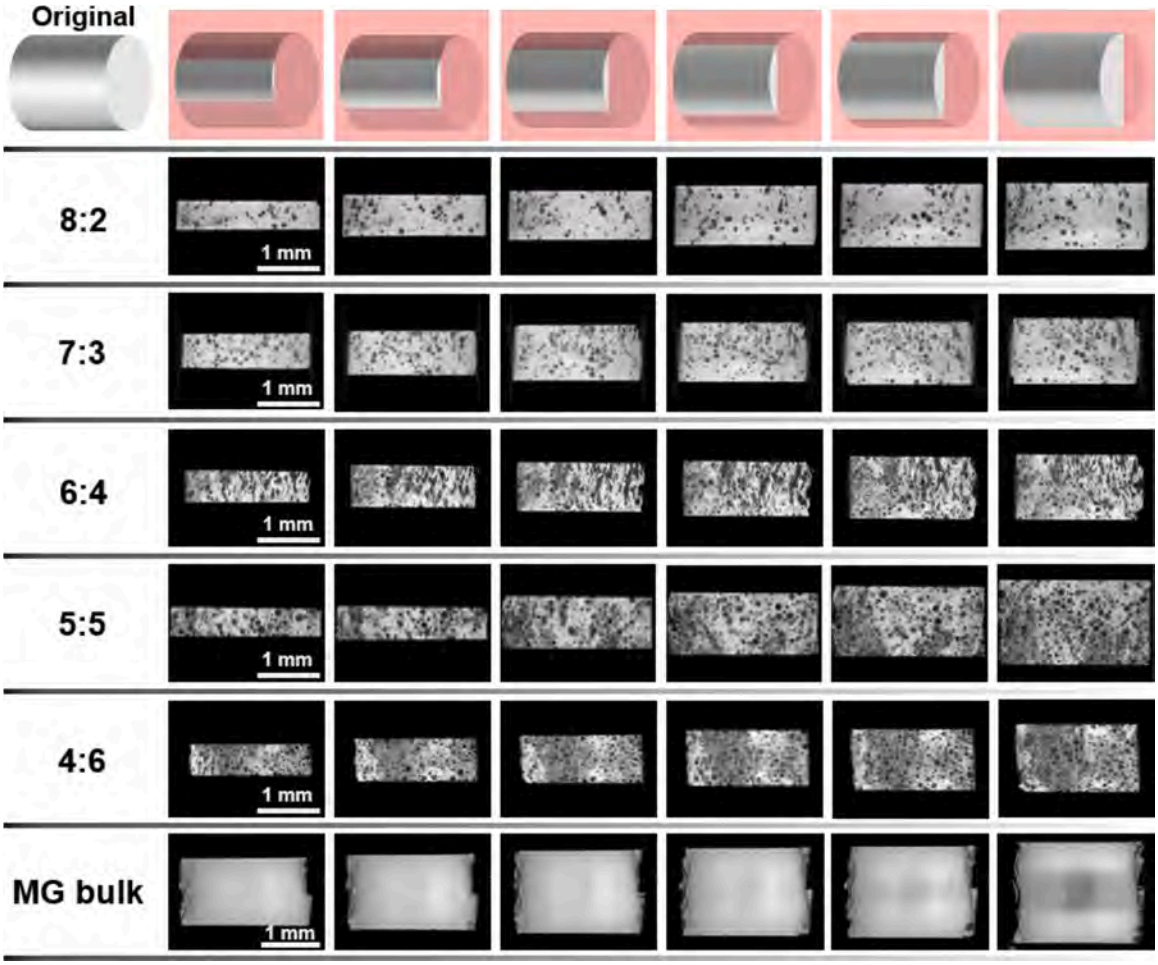

Fig. 4. The cross-sectional CT images at different cutting positions from the outer edge to the center, the illustration shows how the sample was cut during CT.

3.5. *Properties of composite materials*

Compression experiments were performed on amorphous alloys, high-entropy alloys and composite samples to test their macro-mechanical properties like compressive strength, elasticity and plasticity. Furthermore, microhardness tester was applied to determine the micro-mechanical properties of the samples. The results of macroscopic and microscopic mechanical properties are shown in Fig. 5(a-b). From the stress-strain curves obtained by the compression experiments, we can learn that the amorphous alloy exhibits relatively high strength, reaching approximately 800 MPa, while also showing poor plasticity, conforming to the commonness of amorphous alloy. The strength of the high-entropy alloy is low, while simultaneously exhibiting excellent plasticity. With the increase of the proportion of high entropy alloy, the composites present slightly poorer strength and obviously better plasticity, which is in line with initial expectations.

It should be here noted that the strength and plasticity of the composites obtained from ultrasonic vibration (this study) are comparatively larger than those achieved in the composites processed from the supercooled liquid [39]. We assume that the oxide layer on the MG particles formed during ultrasonic vibration process was thinner than during thermo-plastic forming process performed under much higher temperatures, and the oxide layer hindered the bonding between MG and HEA particles, which resulted in comparatively deteriorated mechanical performance of the composites.

The overall view of the 5:5 MGMC sample after the fracture is shown in the inset of Fig. 5(c) as a representative of the fracture behaviour in all studied composites. It can be seen that the failure has occurred by shearing at the plane around 45^{o} with respect to the loading axis, suggesting that the main deformation mechanism is shear banding. To further investigate the fracture behaviour in the 5:5 composite, the morphology of the fracture surfaces are shown in Fig 5(c) and (d). Several shear bands are seen at the surface adjacent to the fracture surface of the as-cast MG (Fig. 5(c)). Furthermore, some dimple or vein-

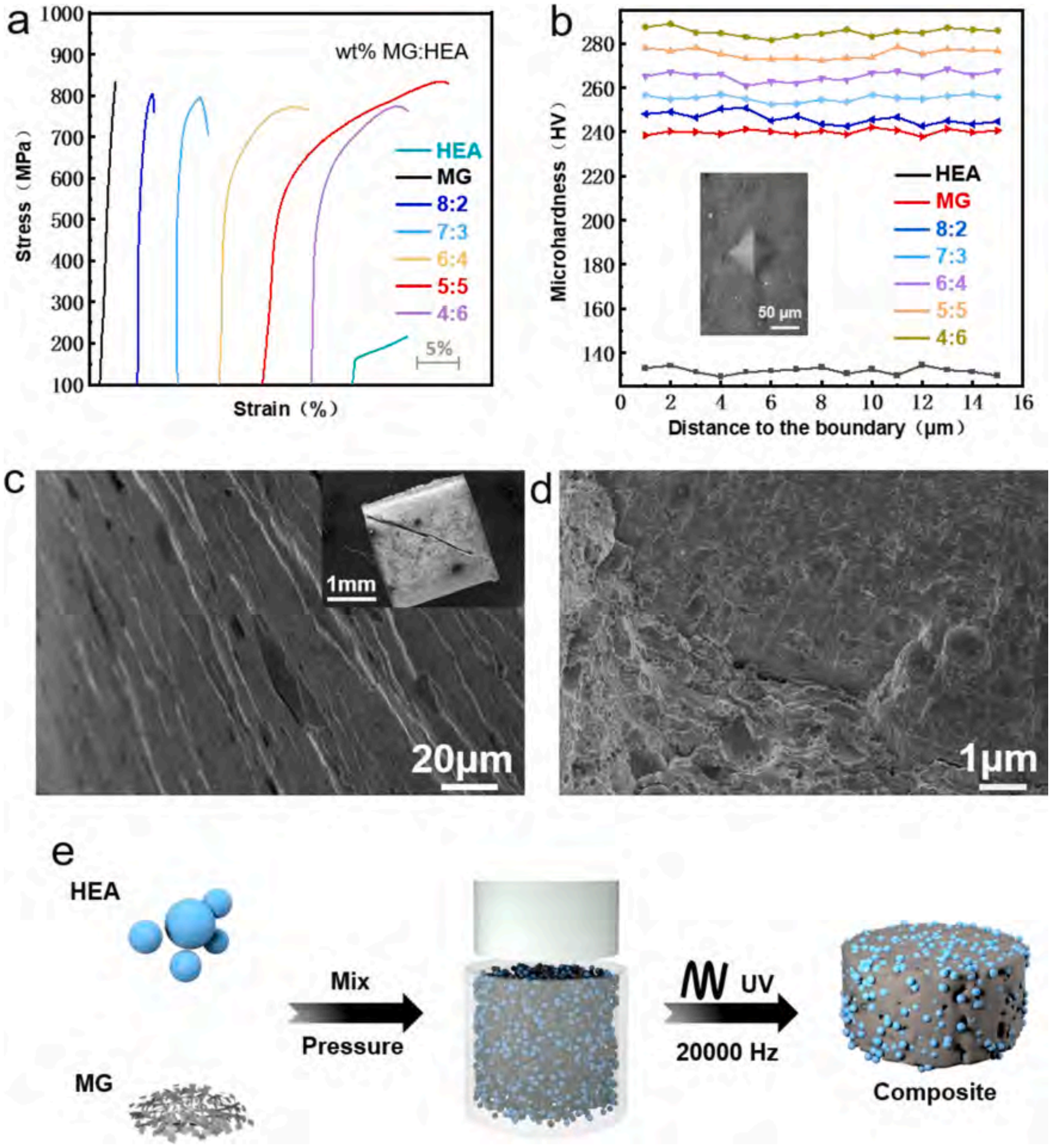

Fig. 5. (a) Compressive stress-strain curves of MG, HEA and their composites. (b) The microhardness of MG, HEA, and the composites. (c)-(d) The shear bands on the surface adjacent to the fracture surface in the 5:5 composite. The inset shows the overall view of the fractured sample. (d) The morphology of the fracture surface of the 5:5 composite. (e) A schematic diagram illustrating the bonding mechanism.

like patterns are observed throughout the fracture surface in Fig. 5(d), which is a characteristic feature in MGs and can be ascribed to the local melting within the primary shear bands induced by the high elastic energy of the instantaneous fracture. In addition, the extended plasticity observed in 5:5 composite might be attributed to the delocalization of shear strain due to the presence of the HEA powders which is associated with multiple shear banding, as observed in Fig. 5(c). The final failure will then occur by the propagation of crack around the HEA powders and the detachment of the HEA particles from the surrounding MG matrix.

The mechanical properties of the composites inherit the advantages of both amorphous alloy and HEA and thus exhibiting tailorable strength and plasticity, which makes the composites competent on some occasions where MG and HEA are not when applied alone and entitles the composites with more application prospects. The results of microhardness test indicate that the microhardness of high entropy alloy is the lowest, coming at nearly 130 HV, followed by amorphous alloy, up to about 240 HV, and notably, the microhardness of each proportion of composites is higher than both amorphous alloy and high entropy alloy, and when high entropy alloy makes up higher proportion in the composites, the hardness of composites rise.

3.6. Bonding Mechanism

The crack of the oxide layer of MG[38] and the transfer among atoms of MG and HEA contribute a lot to the stable bonding of the composites. It is widely accepted that a strong physic bonding of two surfaces requires atoms contact and contaminant free condition. However, it's quite challenging for metals to reach such requirements, which is attributed to the contaminants attracted by high surface energy of metals during processing. One of the typical factors that caused the contaminants is oxygen, which resulted in the formation of a compact oxide layer. The oxide layer plays as a hindrance of the bonding for MG with other materials, hence, it's crucial for MG to break through the barrier of the oxide layer so that to bond with HEA to fabricate their composites. In this study, before ultrasonic vibration was applied to fabricate the composites, the MG and HEA powders were evenly mixed, meanwhile, there remain large amounts of gaps between MG and HEA particles because of no interaction, as seen in Fig. 5(e). With the application of ultrasonic vibration, MG particles were enabled to soften and deform, leading to the elimination of those gaps, which made HEA particles fully wrapped by MG. Furthermore, the oxide layer of MG crashes under high frequency ultrasonic vibration, making elements transfer possible. As seen from Fig. 3(o), the La, Al and Cu elements partly transfer from $La_{55}Al_{25}Ni_5Cu_{10}Co_5$ side towards the $Co_{20}Cr_{20}Fe_{20}Ni_{20}Mn_{20}$ side, and assembly, the Cr, Fe and Mn elements from $Co_{20}Cr_{20}Fe_{20}Ni_{20}Mn_{20}$ side partly transfer to the $La_{55}Al_{25}Ni_5Cu_{10}Co_5$ side, promoting the bonding of MG and HEA, and thus achieving the formation of all of the composites with the unique sandwich-like structure. In this whole process, the application of ultrasonic vibration enabled MG to stick together with HEA like glue[39], and the compressive force from the horn made the composites fairly compact.

4. Conclusion

In summary, by using ultrasonic vibration, we successfully fabricated composites of amorphous and high-entropy alloy under low temperature and low stress conditions. Through tuning the mass ratios of amorphous alloy and high entropy alloy in the composites, the regulation of the compressive strength and plasticity of the composites is achieved. SEM and TEM characterization proves that the composites of all ratios exhibit good bonding quality and there are no defects of pores and cracks existing inside their interior. Our results shed light on the design and fabrication of functional gradient materials containing multiphase and multi-component with specific properties.

CRediT authorship contribution statement

Xiong Liang: Writing – review & editing, Supervision. **Kai Wu:** Resources, Data curation. **Jianan Fu:** Formal analysis, Investigation. **Luyao Li:** Software, Investigation. **Caitao Fan:** Investigation. **Wenxin Wen:** Methodology. **Wenqing Ruan:** Methodology, Funding acquisition. **Shuai Ren:** Methodology. **Zhenxuan Zhang:** Supervision. **Jiang Ma:** Methodology, Writing – original draft.

Declaration of Competing Interest

The authors declare that they have no known competing financial interests or personal relationships that could have appeared to influence the work reported in this paper.

Acknowledgement

The work was supported by the Key Basic and Applied Research Program of Guangdong Province, China (No. 2019B030302010), the National Natural Science Foundation of China (Nos. 51971150, 52122105 and 51871157), Guangdong Basic and Applied Basic Research Foundation (Grant Nr. 2020B1515120092), the National Key Research and Development Program of China (No. 2018YFA0703604). The authors also thank the assistance on microscope observation received from the Electron Microscope Center of the Shenzhen University. Specially, we thank Dr Sajad Sohrabi for his help to the manuscript.

References

[1] B. Lin, X. Bian, P. Wang, G. Luo, Application of Fe-based metallic glasses in wastewater treatment, Mater. Sci. Eng. B 177 (2012) 92–95.
[2] M. Ashby, A. Greer, Metallic glasses as structural materials, Scr. Mater. 54 (2006) 321–326.
[3] J.C. Qiao, Q. Wang, J.M. Pelletier, H. Kato, R. Casalini, D. Crespo, E. Pineda, Y. Yao, Y. Yang, Structural heterogeneities and mechanical behavior of amorphous alloys, Prog. Mater Sci. 104 (2019) 250–329.
[4] J. Schroers, Processing of bulk metallic glass, Adv. Mater. 22 (2010) 1566–1597.
[5] C. Schuh, T. Hufnagel, U. Ramamurty, Mechanical behavior of amorphous alloys, Acta Mater. 55 (2007) 4067–4109.
[6] M.M. Trexler, N.N. Thadhani, Mechanical properties of bulk metallic glasses, Prog. Mater Sci. 55 (2010) 759–839.
[7] A. Inoue, A. Takeuchi, Recent development and application products of bulk glassy alloys, Acta Mater. 59 (2011) 2243–2267.
[8] H. Li, Z. Li, J. Yang, H.B. Ke, B. Sun, C.C. Yuan, J. Ma, J. Shen, W.H. Wang, Interface design enabled manufacture of giant metallic glasses, Sci. China Mater. 64 (2021) 964–972.
[9] R.T. Ott, C. Fan, J. Li, T.C. Hufnagel, Structure and properties of Zr–Ta–Cu–Ni–Al bulk metallic glasses and metallic glass matrix composites, J. NonCryst. Solids 317 (2003) 158–163.
[10] A. Inoue, Stabilization of metallic supercooled liquid and bulk amorphous alloys, Acta Mater. 48 (2000) 279–306.
[11] M.M. Khan, I. Shabib, W. Haider, A combinatorially developed Zr-Ti-Fe-Al metallic glass with outstanding corrosion resistance for implantable medical devices, Scr. Mater. 162 (2019) 223–229.
[12] X. Li, X. Liang, Z. Zhang, J. Ma, J. Shen, Cold joining to fabricate large size metallic glasses by the ultrasonic vibrations, Scr. Mater. 185 (2020) 100–104.
[13] R.L. Narayan, K. Boopathy, I. Sen, D.C. Hofmann, U. Ramamurty, On the hardness and elastic modulus of bulk metallic glass matrix composites, Scr. Mater. 63 (2010) 768–771.
[14] M.Z. Ma, R.P. Liu, Y. Xiao, D.C. Lou, L. Liu, Q. Wang, W.K. Wang, Wear resistance of Zr-based bulk metallic glass applied in bearing rollers, Mater. Sci. Eng. A 386 (2004) 326–330.
[15] Y. Yan, C. Wang, Z. Huang, J. Fu, Z. Lin, X. Zhang, J. Ma, J. Shen, Highly efficient and robust catalysts for the hydrogen evolution reaction by surface nano engineering of metallic glass, J. Mater. Chem. A 9 (2021) 5415–5424.
[16] J. Ma, X. Liang, X. Wu, Z. Liu, F. Gong, Sub-second thermoplastic forming of bulk metallic glasses by ultrasonic beating, Sci. Rep. 5 (2015) 17844.
[17] W. Klement, R.H. Willens, P.O.L. Duwez, Non-crystalline Structure in Solidified Gold–Silicon Alloys, Nature 187 (1960) 869–870.
[18] X. Liang, X.L. Zhu, X. Li, R.D. Mo, Y.J. Liu, K. Wu, J. Ma, High-entropy alloy and amorphous alloy composites fabricated by ultrasonic vibrations,, Sci. China Phys. Mech. 63 (2020), 116111.
[19] B. Cantor, I.T.H. Chang, P. Knight, A.J.B. Vincent, Microstructural development in equiatomic multicomponent alloys, Mater. Sci. Eng. A 375-377 (2004) 213–218.
[20] B. Gludovatz, A. Hohenwarter, D. Catoor, E.H. Chang, E.P. George, R.O. Ritchie, A fracture-resistant high-entropy alloy for cryogenic applications, Science 345 (2014) 1153–1158.

[21] S. Guo, C.T. Liu, Phase stability in high entropy alloys: Formation of solid-solution phase or amorphous phase, Progress in Natural Science: Materials International 21 (2011) 433–446.

[22] S. Guo, C. Ng, J. Lu, C.T. Liu, Effect of valence electron concentration on stability of fcc or bcc phase in high entropy alloys, J. Appl. Phys. 109 (2011), 103505.

[23] Z. Li, K.G. Pradeep, Y. Deng, D. Raabe, C.C. Tasan, Metastable high-entropy dual-phase alloys overcome the strength-ductility trade-off, Nature 534 (2016) 227–230.

[24] D.B. Miracle, O.N. Senkov, A critical review of high entropy alloys and related concepts, Acta Mater. 122 (2017) 448–511.

[25] F. Otto, A. Dlouhý, C. Somsen, H. Bei, G. Eggeler, E.P. George, The influences of temperature and microstructure on the tensile properties of a CoCrFeMnNi high-entropy alloy, Acta Mater. 61 (2013) 5743–5755.

[26] O.N. Senkov, G.B. Wilks, J.M. Scott, D.B. Miracle, Mechanical properties of Nb25Mo25Ta25W25 and V20Nb20Mo20Ta20W20 refractory high entropy alloys, Intermetallics 19 (2011) 698–706.

[27] S. Singh, N. Wanderka, B.S. Murty, U. Glatzel, J. Banhart, Decomposition in multi-component AlCoCrCuFeNi high-entropy alloy, Acta Mater. 59 (2011) 182–190.

[28] M.-H. Tsai, J.-W. Yeh, High-Entropy Alloys: A Critical Review, Mater. Res. Lett. 2 (2014) 107–123.

[29] S.F. Zhao, G.N. Yang, H.Y. Ding, K.F. Yao, A quinary Ti–Zr–Hf–Be–Cu high entropy bulk metallic glass with a critical size of 12 mm, Intermetallics 61 (2015) 47–50.

[30] Y. Zhang, T.T. Zuo, Z. Tang, M.C. Gao, K.A. Dahmen, P.K. Liaw, Z.P. Lu, Microstructures and properties of high-entropy alloys, Prog. Mater Sci. 61 (2014) 1–93.

[31] J.W. Yeh, S.K. Chen, S.J. Lin, J.Y. Gan, T.S. Chin, T.T. Shun, C.H. Tsau, S.Y. Chang, Nanostructured High-Entropy Alloys with Multiple Principal Elements: Novel Alloy Design Concepts and Outcomes, Adv. Eng. Mater. 6 (2004) 299–303.

[32] S.V. Madge, P. Sharma, D.V. Louzguine-Luzgin, A.L. Greer, A. Inoue, New La-based glass–crystal ex situ composites with enhanced toughness, Scr. Mater. 62 (2010) 210–213.

[33] J. Qiao, H. Jia, P.K. Liaw, Metallic glass matrix composites, Mater. Sci. Eng. R Rep. 100 (2016) 1–69.

[34] X. Li, D. Wei, J.Y. Zhang, X.D. Liu, Z. Li, T.Y. Wang, Q.F. He, Y.J. Wang, J. Ma, W. H. Wang, Y. Yang, Ultrasonic plasticity of metallic glass near room temperature, Appl. Mater. Today 21 (2020), 100866.

[35] F. Luo, F. Sun, K. Li, F. Gong, X. Liang, X. Wu, J. Ma, Ultrasonic assisted micro-shear punching of amorphous alloy, Mater. Res. Lett. 6 (2018) 545–551.

[36] J. Ma, C. Yang, X. Liu, B. Shang, Q. He, F. Li, T. Wang, D. Wei, X. Liang, X. Wu, Y. Wang, F. Gong, P. Guan, W. Wang, Y. Yang, Fast surface dynamics enabled cold joining of metallic glasses, Sci. Adv. 5 (2019) eaax7256.

[37] H. Zhao, F. Sun, X. Li, Y. Ding, Y.Q. Yan, X. Tong, J. Ma, H.B. Ke, W.H. Wang, Ultrastability of metallic supercooled liquid induced by vibration, Scr. Mater. 194 (2021), 113606.

[38] W. Chen, Z. Liu, J. Schroers, Joining of bulk metallic glasses in air, Acta Mater. 62 (2014) 49–57.

[39] J. Fu, J. Yang, K. Wu, H.J. Lin, W.N. Wen, W.Q. Ruan, S. Ren, Z.X. Zhang, X. Liang, J. Ma, Metallic glue for designing composite materials with tailorable properties, Materials Horizons (2021) 1690–1699.